

Simulating the neutrino flux from the Spallation Neutron Source for the COHERENT experiment

(COHERENT collaboration)

D. Akimov,¹ P. An,^{2,3} C. Awe,^{2,3} P.S. Barbeau,^{2,3} B. Becker,⁴ V. Belov,^{5,1} I. Bernardi,⁴ M.A. Blackston,⁶ C. Bock,⁷ A. Bolozdynya,¹ J. Browning,⁸ B. Cabrera-Palmer,⁹ D. Chernyak,^{7,*} E. Conley,² J. Daughhetee,⁶ J. Detwiler,¹⁰ K. Ding,⁷ M.R. Durand,¹⁰ Y. Efremenko,^{4,6} S.R. Elliott,¹¹ L. Fabris,⁶ M. Febbraro,⁶ J. Galambos,⁶ A. Gallo Rosso,¹² A. Galindo-Uribarri,^{6,4} M.P. Green,^{3,6,8} M.R. Heath,⁶ S. Hedges,^{2,3} D. Hoang,¹³ M. Hughes,¹⁴ E. Iverson,⁶ T. Johnson,^{2,3} A. Khromov,¹ A. Konovalov,^{1,5} E. Kozlova,^{1,5} A. Kumpan,¹ L. Li,^{2,3} J.M. Link,¹⁵ J. Liu,⁷ K. Mann,⁸ D.M. Markoff,^{16,3} J. Mastroberti,¹⁴ M. McIntyre,¹⁷ P.E. Mueller,⁶ J. Newby,⁶ D.S. Parno,¹³ S.I. Penttila,⁶ D. Pershey,² R. Rapp,^{13,†} H. Ray,¹⁷ J. Raybern,² O. Razuvaeva,^{1,5} D. Reyna,⁹ G.C. Rich,³ D. Rimal,¹⁷ J. Ross,^{16,3} D. Rudik,¹ J. Runge,^{2,3} D.J. Salvat,¹⁴ A.M. Salyapongse,¹³ K. Scholberg,² A. Shakirov,¹ G. Simakov,^{1,5} G. Sinev,^{2,‡} W.M. Snow,¹⁴ V. Sosnovstsev,¹ B. Suh,¹⁴ R. Tayloe,¹⁴ K. Tellez-Giron-Flores,¹⁵ I. Tolstukhin,^{14,§} S. Trotter,⁶ E. Ujah,^{16,3} J. Vanderwerp,¹⁴ R.L. Varner,⁶ C.J. Virtue,¹² G. Visser,¹⁴ T. Wongjirad,¹⁸ Y.-R. Yen,¹³ J. Yoo,¹⁹ C.-H. Yu,⁶ J. Zettlemoyer,^{14,¶} and S. Zhang^{13,14}

¹National Research Nuclear University MEPhI (Moscow Engineering Physics Institute), Moscow, 115409, Russian Federation

²Department of Physics, Duke University, Durham, NC, 27708, USA

³Triangle Universities Nuclear Laboratory, Durham, NC, 27708, USA

⁴Department of Physics and Astronomy, University of Tennessee, Knoxville, TN, 37996, USA

⁵Institute for Theoretical and Experimental Physics named by A.I. Alikhanov of National Research Centre “Kurchatov Institute”, Moscow, 117218, Russian Federation

⁶Oak Ridge National Laboratory, Oak Ridge, TN, 37831, USA

⁷Physics Department, University of South Dakota, Vermillion, SD, 57069, USA

⁸Department of Physics, North Carolina State University, Raleigh, NC, 27695, USA

⁹Sandia National Laboratories, Livermore, CA, 94550, USA

¹⁰Center for Experimental Nuclear Physics and Astrophysics & Department of Physics, University of Washington, Seattle, WA, 98195, USA

¹¹Los Alamos National Laboratory, Los Alamos, NM, 87545, USA

¹²Department of Physics, Laurentian University, Sudbury, Ontario, P3E 2C6, Canada

¹³Department of Physics, Carnegie Mellon University, Pittsburgh, PA, 15213, USA

¹⁴Department of Physics, Indiana University, Bloomington, IN, 47405, USA

¹⁵Center for Neutrino Physics, Virginia Tech, Blacksburg, VA, 24061, USA

¹⁶Department of Mathematics and Physics, North Carolina Central University, Durham, NC, 27707, USA

¹⁷Department of Physics, University of Florida, Gainesville, FL, 32611, USA

¹⁸Department of Physics and Astronomy, Tufts University, Medford, MA, 02155, USA

¹⁹Department of Physics and Astronomy, Seoul National University, Seoul, 08826, Korea

(Dated: March 31, 2022)

The Spallation Neutron Source (SNS) at Oak Ridge National Laboratory is a pulsed source of neutrons and, as a byproduct of this operation, an intense source of pulsed neutrinos via stopped-pion decay. The COHERENT collaboration uses this source to investigate coherent elastic neutrino-nucleus scattering and other physics with a suite of detectors. This work includes a description of our Geant4 simulation of neutrino production at the SNS and the flux calculation which informs the COHERENT studies. We estimate the uncertainty of this calculation at $\sim 10\%$ based on validation against available low-energy π^+ production data.

I. INTRODUCTION

At the Spallation Neutron Source (SNS) at Oak Ridge National Laboratory (ORNL), a pulsed 1.4-MW beam of ~ 1 -GeV protons strikes an approximately 50 cm-long Hg target [1]. The incident protons interact multiple times within the thick target, losing energy and spalling nuclei to create the intended neutrons and byproduct charged pions. The majority of the π^+ come to rest (less than 1% decay in flight) within the thick and dense target, and their stopped decays then give rise to neutrinos with

* Now at: Department of Physics and Astronomy, University of Alabama, Tuscaloosa, AL, 35487, USA and Institute for Nuclear Research of NASU, Kyiv, 03028, Ukraine

† rrapp@andrew.cmu.edu

‡ Now at: South Dakota School of Mines and Technology, Rapid City, SD, 57701, USA

§ Now at: Argonne National Laboratory, Argonne, IL, 60439, USA

¶ Now at: Fermi National Accelerator Laboratory, Batavia, IL, 60510, USA

energies of order tens of MeV:

$$\begin{aligned}\pi^+ &\rightarrow \mu^+ + \nu_\mu \\ \mu^+ &\rightarrow e^+ + \bar{\nu}_\mu + \nu_e.\end{aligned}\quad (1)$$

SNS interactions also produce copious quantities of π^- , but the vast majority ($\sim 99\%$) of these capture on nuclei in the target before decaying and rarely produce neutrinos. The proton beam energy is too low to create substantial numbers of other neutrino-producing decay chains, such as those of K^\pm or η .

To take advantage of this high-intensity pulsed-neutrino source, the COHERENT collaboration has deployed multiple neutrino detectors 20-30 m from the target in the SNS basement corridor known as “Neutrino Alley.” The collaboration has performed the first-ever measurements of the cross section of coherent elastic neutrino-nucleus scattering (CEvNS) with the COH-CsI [2] and COH-Ar-10 detectors [3]. CEvNS measurements are planned on additional nuclear targets (Na and Ge), as well as measurements of several charged-current neutrino-interaction cross sections of interest to nuclear and particle physics and astrophysics [4]. As COHERENT’s cross-section measurements become more precise, they will illuminate physics topics including non-standard neutrino interactions [5, 6], neutrino electromagnetic properties [7–11], nuclear form factors and neutron distributions [12–14], and the detection of supernova neutrinos by both dedicated observatories [15, 16] and next-generation neutrino-oscillation experiments [17–19].

Precise knowledge of the SNS neutrino flux is essential to unlocking the full physics potential of the COHERENT cross-section measurements. The error on the overall normalization of the neutrino flux is the dominant systematic in the Ar results [3] and the second-largest systematic in the initial CsI results [2]. Thanks to updated measurements of the quenching factor in CsI, the neutrino flux is the dominant systematic in the final CsI results [20].

We have built a detailed model of the SNS using the Geant4 Monte Carlo framework [21, 22] to characterize the neutrino flux to the COHERENT detectors and have made it publicly available on Zenodo [23]. In addition to the geometry, the simulation accuracy relies on the underlying implementation of pion production in the Geant4 physics model. Section II describes our validation efforts using four standard physics lists against the available world π^+ -production data. World data, however, are imperfect — Hg-target data are not available at low proton energies, data sets at proton energies near 1 GeV are very limited, and most pion-production cross sections are measured using thin targets that do not replicate the half-meter of dense material the protons at the SNS encounter. Although the existing data are insufficient for a precise validation, we estimate the uncertainty of our simulated flux with the QGSP_BERT physics list to be about 10%. Section III describes our simulation of the SNS, along with our tools for studying the characteristics of the resulting neutrinos. We also discuss the

effect of changes to SNS operating conditions; for example, the incident proton kinetic energy has ranged from 0.83 – 1.011 GeV during COHERENT’s lifetime in Neutrino Alley. Section IV summarizes the properties of our simulated neutrino flux using the selected physics list.

Our SNS simulation has applications to additional nuclear and particle physics experiments proposed at the SNS. In Section V, we present a neutrino-flux simulation based on preliminary design work for a proposed Second Target Station (STS) with a tungsten target; our results suggest that the STS could be a very productive site for next-generation neutrino experiments. Section VI describes the use of our simulation to study π^0 and π^- production at the SNS, relevant to accelerator-based searches for light dark matter. We discuss several future avenues for reducing uncertainties related to the SNS neutrino flux in Section VII and conclude in Section VIII.

II. VALIDATION OF SIMULATION PHYSICS

We investigated four standard physics models (or “physics lists”) as implemented in Geant4.10.06.p01: FTFP_BERT, QGSP_BERT, QGSP_BIC, and QGSP_INCLXX. With all SNS protons well below 10 GeV, the differences in the underlying string models of FTFP_BERT and QGSP_BERT were found to be negligible; in this work we focus only on QGSP_BERT. We note here that the plots within this section use natural units, such that $c = 1$.

Each candidate for our physics list models nuclear structure in a specific way. With an implementation of the classical Bertini Cascade model [24] for incident hadrons below 3 GeV, QGSP_BERT is a favored model for the production of hadrons (and subsequently, neutrinos) with its treatment of the nucleus as a gas of nucleons that can be solved on average using the Boltzmann equation for a projectile moving through the gas [25]. The QGSP_BIC physics list differs only for protons and neutrons, for which it implements a Binary Cascade and models the nucleus as an isotropic sphere. In this model, the nucleons are placed at specific positions that projectiles can interact with individually, and each nucleon carries a random momentum between zero and the Fermi momentum [26]. Finally, QGSP_INCLXX extends the Liege Intranuclear Cascade model [27] benchmarked against spallation studies below 3 GeV [28] by modeling the nucleus in a very similar manner to QGSP_BIC, but adding the possibility to emit nucleon clusters that can cause secondary reactions after a projectile interacts with the nucleus. Both QGSP_BIC and QGSP_INCLXX require increased computation time to model the interactions of projectiles with more massive nuclei (compared to QGSP_BERT) [29].

In prior estimations the COHERENT collaboration has used the QGSP_BERT physics list with an assigned 10% uncertainty on any flux predictions coming from

simulation efforts. This estimate was informed by prior studies using an implementation of the Bertini model in the LAHET Monte Carlo framework [30] to make predictions for the LSND and KARMEN experiments [31–33]. World data at the time of their investigation did not agree with LAHET predictions, and LAHET predictions that were renormalized to match available data were lower than Geant4 predictions [31, 34, 35]. The 10% systematic was assigned to our neutrino flux calculations to conservatively account for this discrepancy [2].

Since the lack of pion-production data from 1 GeV proton-mercury interactions prevents a direct comparison, our choice of physics model must be validated via other targets, usually at higher energies. In Section II A we compare the total π^+ -production cross section to the Norbury-Townsend parameterization developed to match data from proton-nucleus and nucleus-nucleus collisions [36]. Not included in the development of the Norbury-Townsend parameterization, however, are newer results focusing on double-differential measurements, such as those from the thin-target HARP experiment [37]. We detail our validations against the HARP measurements in Section II B. Older experiments also collected double-differential pion-production data at energies closer to the SNS, such as Abaev *et al.* in 1989 [38], but their data have a very limited angular coverage. We use these data sets to check the model behavior at lower proton energies (Section II C) since they cannot constrain our total neutrino flux. We discuss the effects of modeling the thick target of the SNS in Section II D and interpret all of our validation work to estimate a neutrino flux systematic for COHERENT in Section II E.

A. Norbury-Townsend Parameterization

This empirical function was developed to parametrize pion-production data from proton-nucleus and nucleus-nucleus interactions measured by Nagamiya *et al.* [39]. While developed in the right energy range for SNS operations at ~ 1 GeV, π^+ production data was only taken for subsets of Ne + NaF, Ne + Cu, Ne + Pb, C + C, C + Pb, Ar + KCl, Ar + Pb for 0.4, 0.8, and 2.1 GeV per incident nucleon — only π^- production data was available from the proton-nucleus studies [36]. Although our focus is π^+ production in this work, we note that future effort to check the candidate physics models against the parameterizations for π^- and π^0 production will be useful to validate the flux predictions for dark-matter-producing particles at the SNS that we present in Section VI.

The Norbury-Townsend parameterization of the π^+ production cross section (σ_{π^+} in mb) is shown in Eqn. 2, where A_t is the number of target nucleons, and E_i (in GeV) is the energy per incident nucleon:

$$\sigma_{\pi^+} = \frac{A_t^{2.2/3}}{0.00717 + 0.0652 \frac{\log(E_i)}{E_i} + \frac{0.162}{E_i^2}}. \quad (2)$$

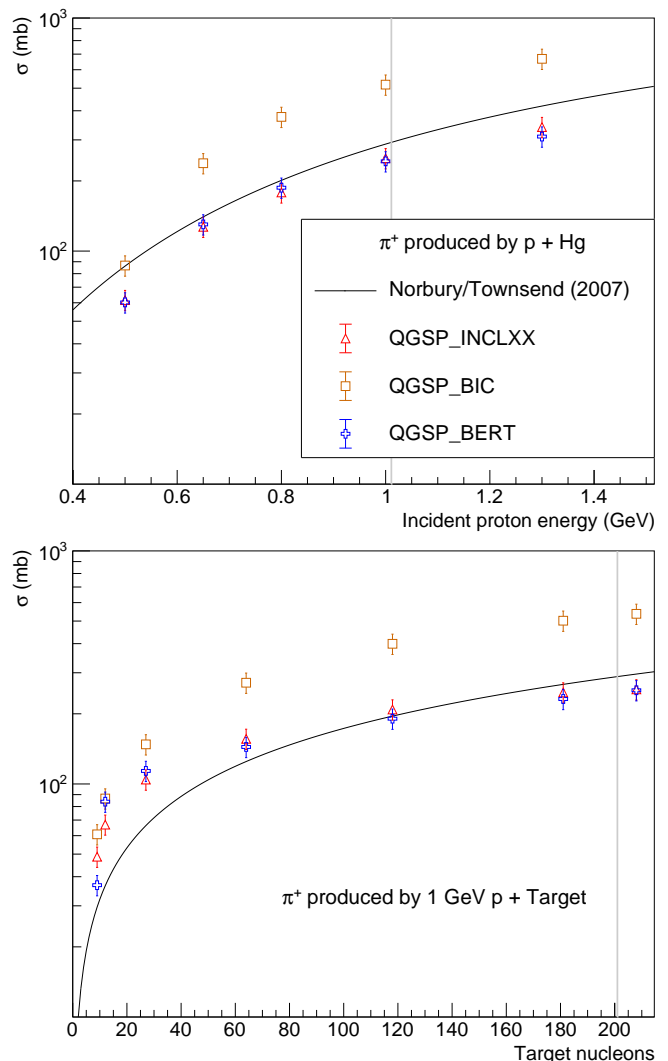


FIG. 1. Comparisons of the Norbury-Townsend parameterization and Geant4 model predictions of total pion-production cross section. Top: Dependence of total cross section on incident proton energy for a mercury target. The vertical line indicates the current SNS operating energy of 1.011 GeV, but COHERENT still sees π^+ production at energies below this value due to proton energy loss within the thick target (see Fig. 16). Bottom: Dependence of total cross section on target nucleus for a proton energy of 1 GeV. The vertical line represents a mercury target.

Using a thin simulated target ($5 \times 5 \times 0.5$ cm³) with specified isotope, molar mass, and density, we counted the total number of pions produced. We then scaled this event rate by our simulated number of target nuclei and incident flux of protons to convert to a total cross section prediction. Figure 1 shows comparisons of these results to the parameterization across incident energies (top) and target nucleus (bottom), with a 10% uncertainty applied to the cross sections from each potential physics list.

B. HARP and HARP-CDP

HARP, the Hadron Production Experiment (PS214), operated at CERN’s Proton Synchrotron from 2000 to 2002. With a nearly 4π acceptance and incident proton momentum range from 1.5 GeV/c to 15 GeV/c, HARP measured 7 different solid targets (Be, C, Al, Cu, Sn, Ta, Pb) as well as 4 cryogenic liquid targets (H_2 , D_2 , N_2 , O_2). The HARP collaboration disagreed on their TPC calibrations causing a subgroup, HARP-CDP, to promote different calculations of pion momenta and identification of protons and pions [40]. Both of these differences impact the final analysis, such that HARP-CDP reports lower cross sections than the HARP analysis. In this paper, both sets of cross section results were checked against our Monte Carlo simulations.

Data were not collected for incident protons at 1 GeV; therefore we compare to the HARP and HARP-CDP analyses of 3 GeV/c data on a large range of nucleon numbers: Be [41], C [42, 43], Al [41, 44], Cu [42], Sn [42, 45], Ta [46, 47], and Pb [41, 48]. We follow a similar procedure to our Norbury-Townsend comparisons and simulate monoenergetic protons with 2.205 GeV of kinetic energy (calculated from the 3 GeV/c beam momentum) incident on a thin target ($5 \times 5 \times 0.5 \text{ cm}^3$), though here counting pions produced per pion momentum and production angle rather than total number of pions. We then scale the stored event rates by our simulated target details to convert to a doubly differential cross section prediction from each simulation model. Figure 2 illustrates the direct comparison of our simulation to the HARP and HARP-CDP results for 3 GeV/c $p + {}^{208}\text{Pb}$. The simulation error bands combine statistical uncertainty with the estimated 10% systematic uncertainty on the simulation prediction.

Since the Geant4 models predict the HARP and HARP-CDP data better in some bins than others, we integrate away the angular or momentum dependence to compare singly differential cross sections. The comparisons shown in Fig. 3 integrate our simulation prediction over the angular region of the HARP analysis; there is less than a 1% difference from the simulation prediction integrated over the HARP angular region and over the HARP-CDP angular region, so we show HARP-CDP data on the same axes.

The SNS mercury target is thick and dense enough to stop the majority of the pions regardless of production angle or momentum. Therefore, to a very good approximation, we require only the total cross section to simulate the neutrino production. We integrate away the dependence on both production angle (350 - 2150 mrad) and momentum (0.1 - 0.8 GeV) and show the total cross-section comparisons to both HARP and HARP-CDP data in Fig. 4. The ratio of the Geant4 model prediction to the HARP or HARP-CDP result determines how well we predict the data.

C. Low-energy pion-production data

Using the proton synchrotron at the Leningrad Nuclear Physics Institute (Gatchina, Russia) with a beam kinetic energy of $997 \pm 5 \text{ MeV}$, Abaev *et al.* measured pion production on 16 different isotope targets at 0° and 57.8° with 0.01 steradian angular acceptance [38]. We compare to a range of nucleon numbers, but we exclude comparisons to different isotopes of the same nucleus in this work as no significant difference between different isotopes was found in the cross sections from data or simulation. The double-differential comparisons of the Geant4 models to Abaev *et al.* are shown in Fig. 5, and the momentum-integrated comparisons are shown in Fig. 6.

D. Secondary particle interactions

The pion-production model of QGSP_BERT has the best agreement for thin-target data, but we must also model the proton energy loss and the interactions of any secondary particles that are produced. For example, π^+ scattering will affect our predictions on how many π^+ decay at rest, and pion interactions such as charge exchange or absorption will impact the number of π^+ that decay into neutrinos. In our simulations of the SNS, $\sim 25\%$ of the π^+ tracks that are produced end in non-decay processes (labeled “pi+Inelastic” in Geant4). Pions and other secondary hadrons created at the SNS are well below 10 GeV and use the default cross-section tables implemented in the Bertini Cascade model (primarily the Baranshenkov and Glauber-Gribov parameterizations) [24]. We do not perform any specific validation of these processes in this work.

E. Interpretation

We are not aware of any data from $p+\text{Hg}$ and very few data sets exist at these energies, so this work is intended as a cross-check of prior estimates rather than as a derivation of our neutrino-flux systematic. We choose to simulate the SNS using QGSP_BERT, and find that a 10% uncertainty is consistent with our validation studies. In particular, QGSP_BERT is the only model which agrees at the 10% level with the cross section measurements of both HARP and HARP-CDP; the other lists overpredict the HARP-CDP data. The validation against the Norbury-Townsend parameterization further demonstrates an overall normalization problem with QGSP_BIC, despite noteworthy agreement in the tails of the 57.8° Abaev measurement. While QGSP_INCLXX is acceptable, QGSP_BERT has better agreement with the data and the added bonus of being more computationally efficient. We note that while the momentum-integrated Abaev data may disagree with QGSP_BERT predictions at more than the 10% level, similar disagreement is shown in the bottom panel of Fig. 3 for single points of the

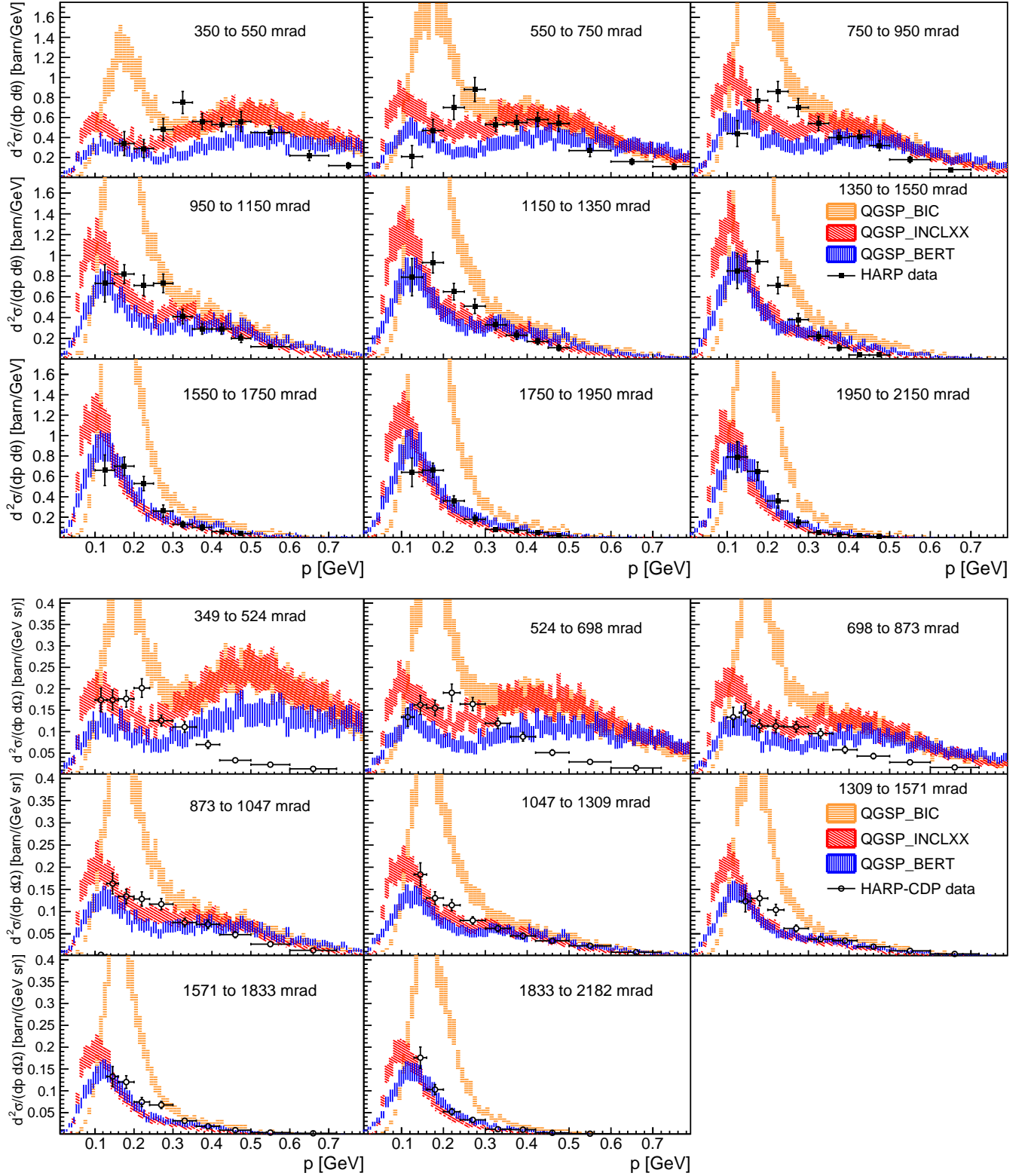


FIG. 2. Comparisons of double-differential cross sections of π^+ production from 3 GeV/c $p+^{208}\text{Pb}$ as predicted by the different Geant4 physics lists to the measurements from HARP (top) and HARP-CDP (bottom). The error band shown for each physics list is a 10% uncertainty. We highlight ^{208}Pb because, among HARP targets, this isotope is closest in mass to the SNS mercury target.

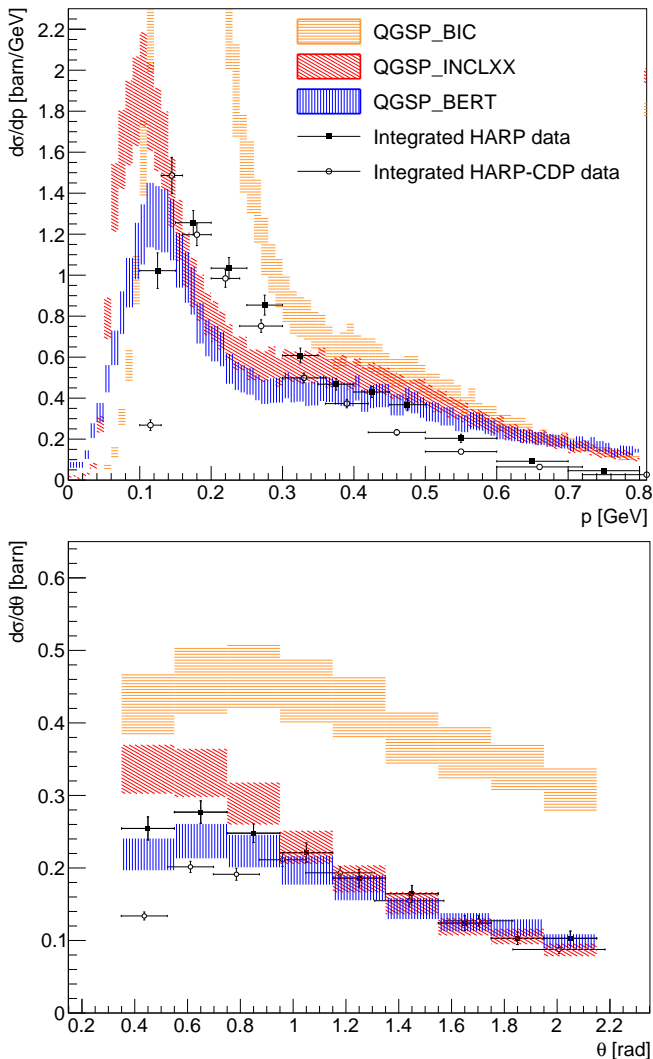


FIG. 3. Comparison of measured differential cross sections of π^+ production from 3 GeV/c $p+^{208}\text{Pb}$ to Geant4 physics lists. Top: HARP and HARP-CDP data were integrated over their respective angular regions and compared to simulation integrated from 350 to 2150 mrad in production angle. Bottom: HARP and HARP-CDP data were integrated from 0.1 to 0.8 GeV/c in momentum and compared to simulation integrated on the same region.

momentum-integrated HARP and HARP-CDP comparisons; it is only after an additional integration over angle that good agreement is achieved. Ultimately, the limited angular coverage of the Abaev data limits our ability to investigate this effect.

In light of these studies and prior work using the Bertini cascade for neutrino flux calculations [31–33, 49, 50], we continue to use QGSP_BERT with a 10% uncertainty on the flux predictions that come from our Geant4 simulations. This systematic cannot be improved without new measurements, and we describe future avenues for reducing this uncertainty in Section VII.

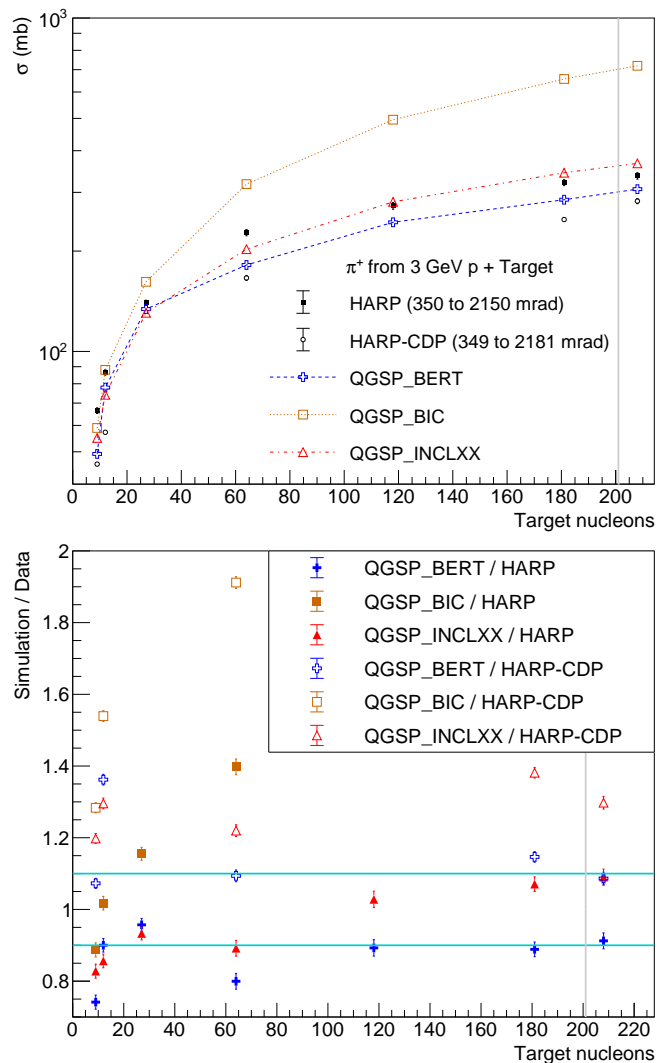


FIG. 4. Top: The HARP data and Geant4 model predictions of the pion-production cross section integrated over 350 - 2150 mrad and 0.1 - 0.8 GeV. The HARP-CDP data are also shown but are integrated over 349 - 2181 mrad and 0.1 - 0.8 GeV. Bottom: Ratio of the Geant4 simulated predictions to the central values of the data, plotted with an uncertainty on all three simulations shown as data error / central value (the HARP-CDP error bars are small enough to be hidden by the points themselves). The horizontal cyan lines mark a $\pm 10\%$ uncertainty band. The vertical gray line on each plot represents a mercury target.

III. MODELING THE SPALLATION NEUTRON SOURCE IN GEANT4

The design of the SNS target and moderator suite was optimized for neutron production and related science [1]. We define simplified components of the SNS target monolith that are expected to contribute to pion production or to the stopping of pions and muons. The simplification process is demonstrated in the top panel of Fig. 7, where the technicalities of the target vessel are reduced

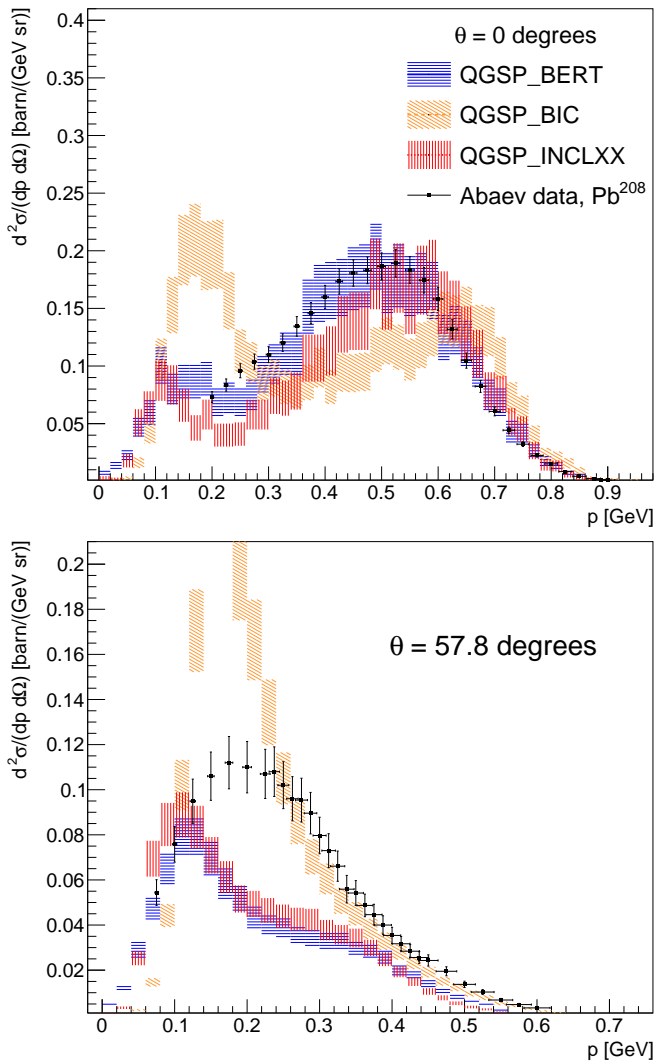


FIG. 5. Comparisons of double-differential cross sections of π^+ production from 1 GeV $p+^{208}\text{Pb}$ at 0° and 57.8° as predicted by the different Geant4 physics lists to the measurements from Abaev *et al.*

to the mercury-containing region shaded red. The bottom panel of Fig. 7 highlights the target monolith and Neutrino Alley to illustrate the structures we build into our model. The details of our SNS model, along with their relative contributions to the overall π^+ production, are shown in Table I, and the full visualization of our simple model is shown in Fig. 8.

Though most of the components we simulate are essentially unchanged during running despite routine maintenance and possible replacements, we must carefully consider the proton beam window (PBW) separating the vacuum of the accelerator from the target. Each proton must pass through the PBW, resulting in both proton energy loss and pion production as a result of interactions in the thin window. The PBW is routinely replaced due to radiation damage, and two different PBW designs have been in use during COHERENT's live-time in Neutrino

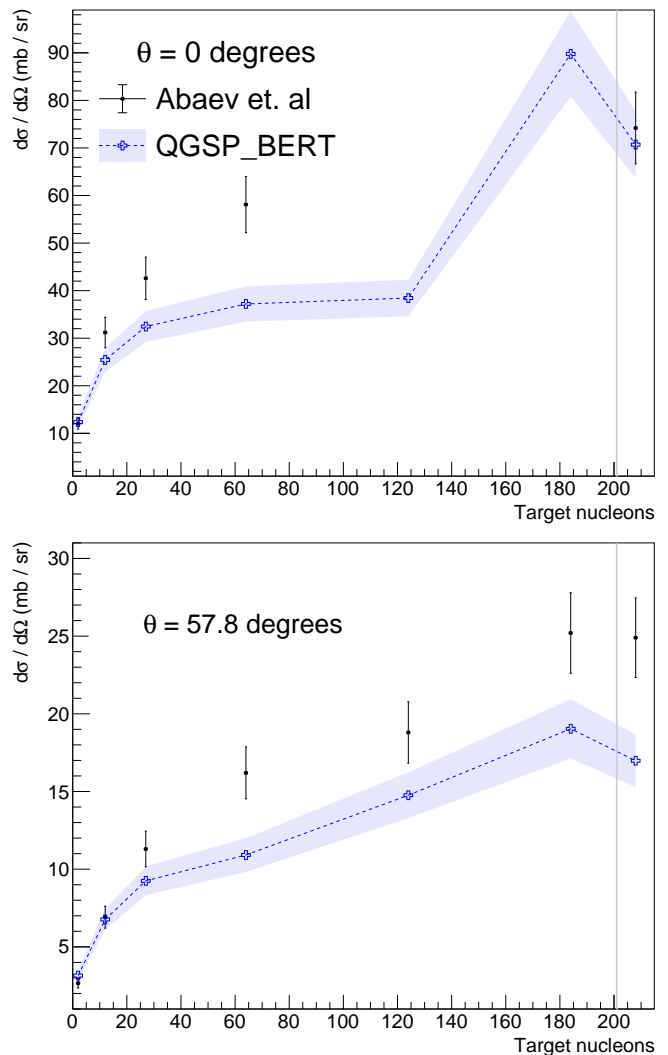


FIG. 6. Comparisons of differential cross sections at 0° and 57.8° as predicted by QGSP_BERT to measurements by Abaev *et al.* The vertical gray lines represent a mercury target.

Alley. A two-layered film design using Inconel, a nickel-based alloy trademarked by the Special Metals Corporation [52], with water cooling between the films, was used from the initial SNS production runs until January 11, 2017. An aluminum plate design with 50 drilled pipes for water cooling was in place until the latest replacement reverted back to an Inconel PBW on April 7, 2020. Figure 9 illustrates both PBW designs as modeled in our Geant4 geometry.

The SNS accelerates protons into an accumulator ring, which ensures that a focused beam of monoenergetic protons is directed on to the target. This beam is magnetically spread to prevent overheating of the proton beam window and target casing [53]; we introduce a uniformly distributed source using a prior measurement of the beam profile at the target [54] to account for this. Our simulated profile is illustrated in the bottom panel of Fig. 9

TABLE I. An overview of components in our Geant4 model that contribute to the overall pion-production. We also include the fraction of π^+ , and therefore ν , our simulations produce as a result of each volume. We report the dimensions from the perspective of the beamline as either Width \times Height \times Depth or Diameter (\varnothing) \times Height. The depth of the Inconel proton beam window (PBW) is an approximation (indicated by an *) of 3 cm, which includes some amount of vacuum immediately before and after the window as a result of the curvature.

| Component | Material | Dimensions | π^+ contributed | |
|--------------------|--|---|---------------------|-------------|
| | | | Aluminum PBW | Inconel PBW |
| Target | Hg | $39.9 \times 10.4 \times 50.0 \text{ cm}^3$ | 94.12% | (90.91%) |
| Target Casing | Steel | $40.9 \times 11.4 \times 51.0 \text{ cm}^3$ | 0.20% | (0.56%) |
| Inner Plug (2) | Be, D ₂ O | 70.0 cm \varnothing , 45 cm | 0.19% | (0.23%) |
| Moderator (4) | H ₂ (3), H ₂ O (1) | $4.0 \times 13.9 \times 17.1 \text{ cm}^3$ | 0.01% | (0.01%) |
| Reflector | Steel, D ₂ O | 108 cm \varnothing , 101.6 cm | 0.99% | (1.34%) |
| Beamline Shielding | Steel | $64.8 \times 54.6 \times 200.0 \text{ cm}^3$ | 0.93% | (1.72%) |
| Target Room | Steel | 1002 cm \varnothing , 950.8 cm | 0.00% | (0.14%) |
| Aluminum PBW | Al-6061, H ₂ O | $29.8 \times 14.6 \times 0.02 \text{ cm}^3$ | 2.77% | (—) |
| Aluminum Beamline | Air | $29.8 \times 14.6 \times 200.0 \text{ cm}^3$ | 0.79% | (—) |
| Inconel PBW | Inconel-718, H ₂ O | $26.7 \times 12.7 \times 3.0 \text{ cm}^{3*}$ | — | (4.32%) |
| Inconel Beamline | Air | $26.7 \times 12.7 \times 200.0 \text{ cm}^3$ | — | (0.77%) |

to show its size relative to the beam window designs and target.

We specify the particles for the simulation to track, typically ν_x , π^\pm , μ^\pm , K^\pm , η , p , and n , to ensure that we do not truncate any possible neutrino production chain. Using the Monte Carlo framework of Geant4 and the QGSP_BERT physics model chosen in Section II, we observe which particles and interactions are responsible for generating the SNS neutrino flux. The predictions we make are dependent on our chosen physics model; for example, the QGSP_BIC nuclear model predicts some production of the η meson given 1 GeV incident protons while other models do not.

IV. SIMULATED NEUTRINO FLUX FOR THE FIRST TARGET STATION

Figure 10 shows the energy and timing spectra for each neutrino flavor present in the simulation using the QGSP_BERT physics list to simulate incident protons with 1 GeV of kinetic energy on the SNS geometry with an aluminum PBW. We find that the SNS ν flux predictably demonstrates the characteristics of a pion decay-at-rest source such as the monoenergetic ν_μ at ~ 30 MeV from π^+ decay at rest and $\bar{\nu}_\mu$ and ν_e following the Michel spectra predicted from the three-body μ^+ decay at rest (DAR). Variations from these spectra include decays in flight (DIF), decays in orbit (DIO), and μ^- capture. We also observe some contribution from decay-at-rest kaons, notably in the ν_μ spectrum at ~ 240 MeV, but due to the small phase space available to produce these more massive particles, kaons have an almost negligible contribution to the SNS neutrino flux. Ultimately, this simulation predicts a decay-at-rest neutrino source with greater than 99% purity, with the exact creation process and par-

ent particle breakdown shown for the aluminum PBW in Table II.

Using 1 GeV protons incident on our SNS geometry from behind the PBW, our simulations predict 0.262 neutrinos per proton on target. We find that our model of the SNS neutrino flux is primarily comprised of ν_μ , $\bar{\nu}_\mu$, and ν_e (each greater than $0.087 \nu_X/\text{POT}$, where $X = \mu, \bar{\mu}, e$) with a small contribution of $\bar{\nu}_e$ ($0.0001 \bar{\nu}_e/\text{POT}$, not considering the activation of materials near the target). We also see a small flux of low-energy $\bar{\nu}_e$ from neutron β -decay that we neglect in this work, with the intention of performing a dedicated study of radioactive products produced as a result of SNS operations in the future.

COHERENT deployed detectors at the SNS prior to the accelerator systems reaching 1 GeV, so data taken at lower energies (~ 850 MeV) must also be understood. The upcoming Proton Power Upgrade [55] will prepare the SNS for the planned Second Target Station (described in Section V) by improving the accelerator. The upgrade will see the SNS operate at a more intense 2.0 MW, with 1.3 GeV incident protons by 2024. We use this simulation to study the dependence of the neutrinos produced on the incident proton energy and to develop an approach to account for changes to SNS operations over a run period. Figure 11 shows the energy dependence for both the total neutrino production and the fraction of neutrinos produced by the π^+ decay chain, and the parameters for each of the fits are listed in Table III. This figure also demonstrates that while there are minimal differences in total neutrino production between the two PBW designs, the differences in the relative contribution of pion production resulting from interactions with the PBW (see Table I) can impact the stopping power of the SNS. The neutrino luminosity from the SNS given particular operating conditions can then be calculated as

TABLE II. A breakdown of the processes and parent particles which create neutrinos for 1 GeV protons at the SNS with an aluminum PBW. The creation processes are classified as decay at rest (DAR), decay in flight (DIF), μ^- capture, or decay in orbit (DIO). We include significant figures here to sum to 100% given the small contributions outside of the π^+ DAR chain.

| | ν / POT | Creation Process | | | | Parent Particle | | |
|-----------------|-------------|------------------|--------|-------------|-------------|--------------------|--------------------|---------|
| | | DAR | DIF | μ^- Cap | μ^- DIO | π^+ or μ^+ | π^- or μ^- | K^+ |
| ν_μ | 0.0875 | 98.940% | 0.779% | 0.196% | 0.084% | 99.7185% | 0.2812% | 0.0003% |
| $\bar{\nu}_\mu$ | 0.0875 | 99.718% | 0.282% | — | — | 99.7187% | 0.2813% | — |
| ν_e | 0.0872 | 99.999% | 0.001% | — | — | 99.9999% | — | 0.0001% |
| $\bar{\nu}_e$ | 0.0001 | — | 0.331% | — | 99.669% | — | 100% | — |

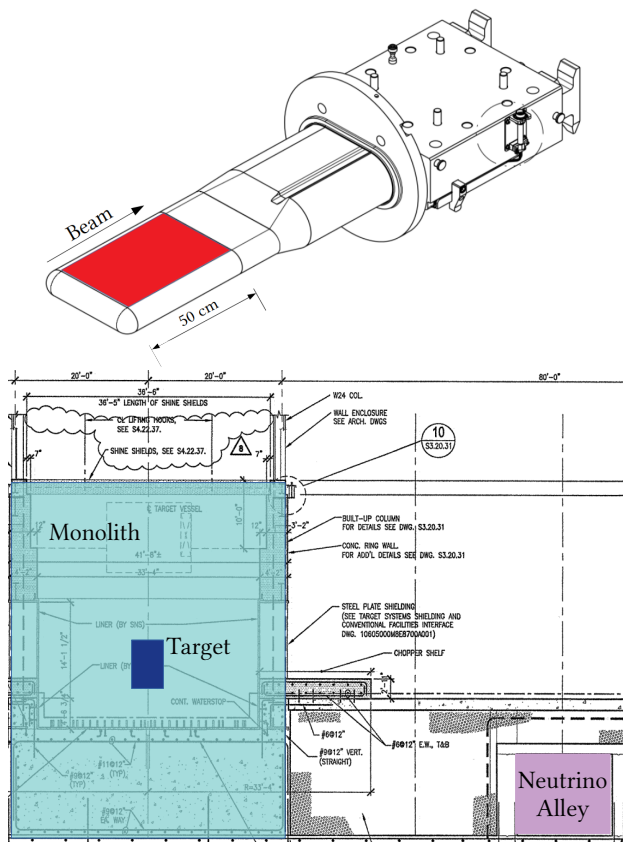


FIG. 7. Top: ORNL technical drawing of the target vessel. The red section highlights the main Hg target as implemented in our Geant4 model. Bottom: A portion of an ORNL technical drawing illustrating the target hall, with pieces in our Geant4 model highlighted. The outer shaded cyan is the concrete monolith, with the inner indigo representing the steel containing the Hg target and moderators. In the bottom right corner, the shaded purple shows the location of Neutrino Alley relative to the target monolith [51].

$$\frac{\nu}{t} = \frac{\nu}{\text{POT}} \frac{\text{POT}}{t} = \frac{\nu}{\text{POT}} \frac{E_{\text{total}}}{E} \frac{1}{t} = F(E) \frac{P}{E}, \quad (3)$$

where E is the kinetic energy per proton, $F(E)$ is the fraction of ν produced per proton on target with incident kinetic energy E , E_{total} is the combined energy of all

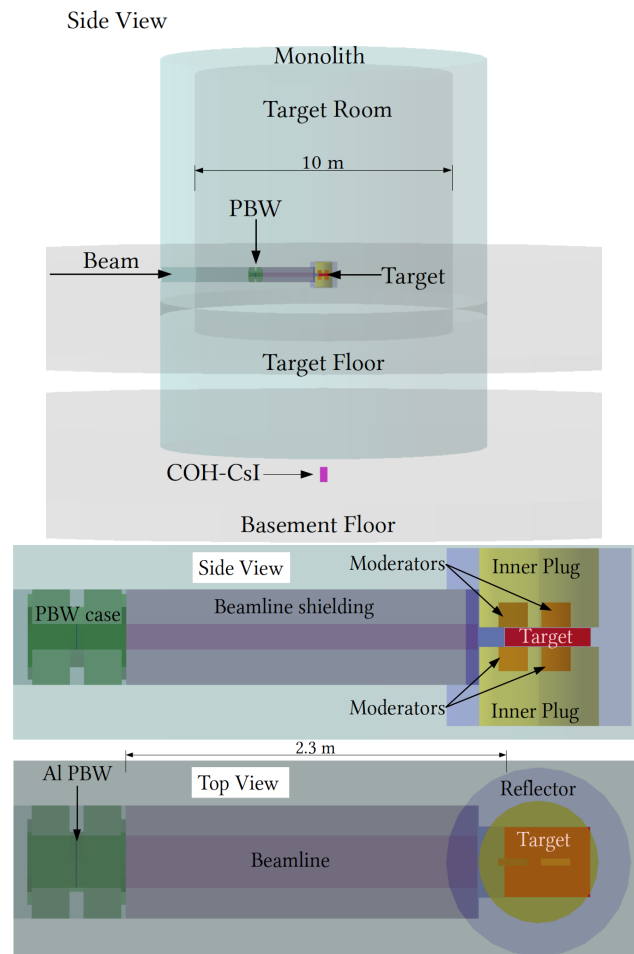


FIG. 8. Our Geant4 model of the SNS, simplified from ORNL technical drawings. Top: The full Geant4 world, highlighting the monolith relative to the location of COH-CsI in Neutrino Alley. Bottom: A view inside the outer monolith illustrating the target, neutron moderator suite, proton beam window, and beamline shielding.

protons incident on the target in time t , and P is the SNS beam power (E_{total}/t). Figure 11 demonstrates that $F(E)$ can be estimated as a cubic polynomial in E with parameters defined in Table III, for E between 0.775 and 1.425 GeV. Plugging this into Eqn. 3, we find a general expression for the SNS neutrino luminosity:

TABLE III. Fit parameters for the proton-energy dependence studies using both beam window designs. The three parameters for the cubic fits used in Eqn. 3 ($F(E) = p_3 E^3 + p_2 E^2 + p_1 E + p_0$) are illustrated in the top panel in Fig. 11, while the two parameters for the linear fits ($mE + b$) are illustrated in the bottom panel. The fit uncertainties do not consider the overall 10% systematic.

| Design | p_3 [GeV^{-3}] | p_2 [GeV^{-2}] | p_1 [GeV^{-1}] | p_0 | b | m [GeV^{-1}] |
|--------------|-----------------------------|-----------------------------|-----------------------------|----------|-----------|---------------------------|
| Aluminum PBW | 0.28(2) | -1.12(6) | 1.79(6) | -0.68(2) | 99.99(1) | -0.48(1) |
| Inconel PBW | 0.27(2) | -1.09(6) | 1.75(6) | -0.67(2) | 100.04(1) | -0.53(1) |

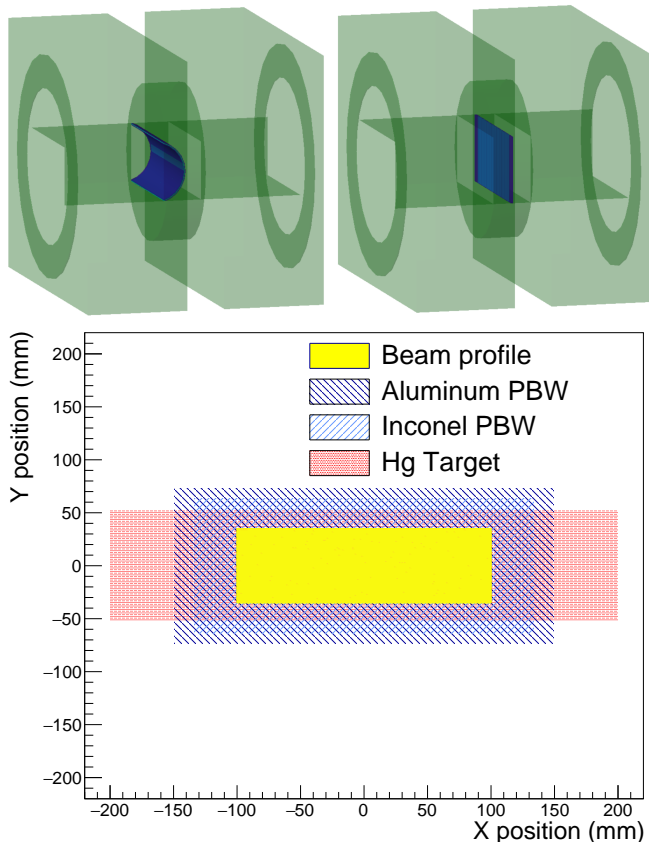


FIG. 9. Top left: Geant4 mockup of the dual-film Inconel PBW, with water cooling between the two films. Top right: Geant4 mockup of the aluminum plate PBW, with 50 vertical pipes for water cooling. Bottom: The position of incident protons shown relative to the profiles of the different PBW designs and Hg target.

$$\frac{\nu}{t} = P \left(p_3 E^2 + p_2 E + p_1 + \frac{p_0}{E} \right). \quad (4)$$

Using this functional form and typical pre-upgrade operational parameters of 1.4 MW (7.0 GWhr/yr) and incident protons with 1 GeV of kinetic energy, we calculate 2.36×10^{15} neutrinos produced per second while the SNS is running. Estimating this production as an isotropic point source, we calculate a neutrino flux of $4.7 \times 10^7 \nu \text{ cm}^{-2} \text{ s}^{-1}$ at 20 meters from the target center (the approximate location of the first CEvNS measure-

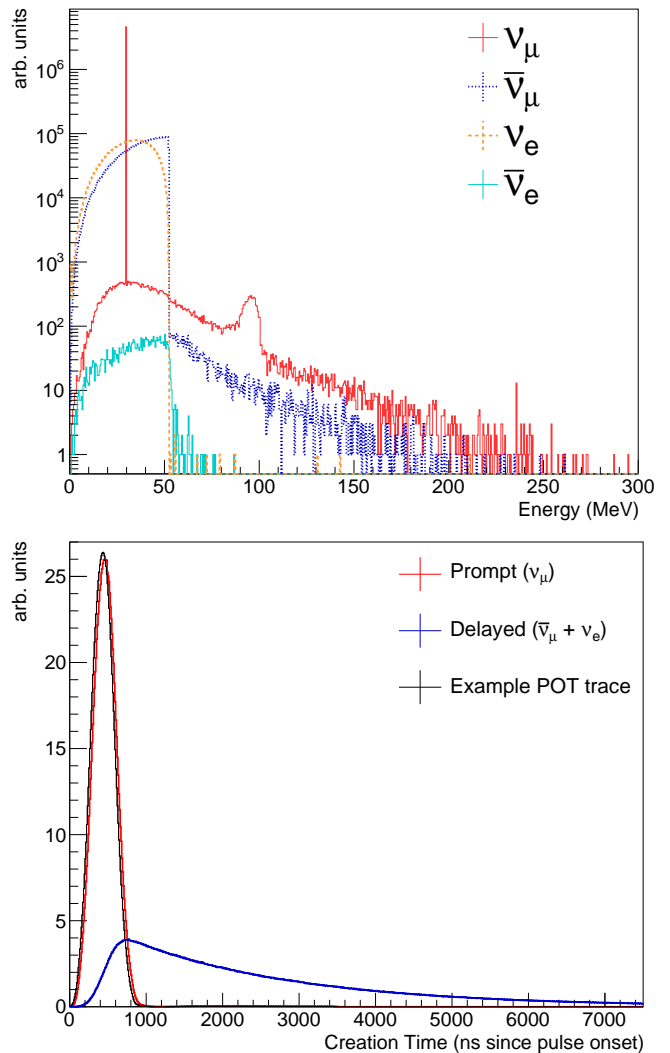


FIG. 10. Distributions of neutrino energy (top) and creation time (bottom) produced at the SNS, using QGSP_BERT to model the interactions of 1 GeV protons incident on the aluminum PBW geometry. We convolve the single proton output of our simulations with the proton-on-target trace.

ments in COH-CsI). Using the nominal SNS running time of 5000 hours per year, the SNS sees 1.58×10^{23} POT per year, with a ν luminosity of $4.25 \times 10^{22} \nu$ per year, or a flux of $8.46 \times 10^{14} \nu \text{ cm}^{-2} \text{ yr}^{-1}$ at 20 m from the target.

We also study the creation positions and momenta of the neutrinos, shown in Fig. 12. The volumes and ma-

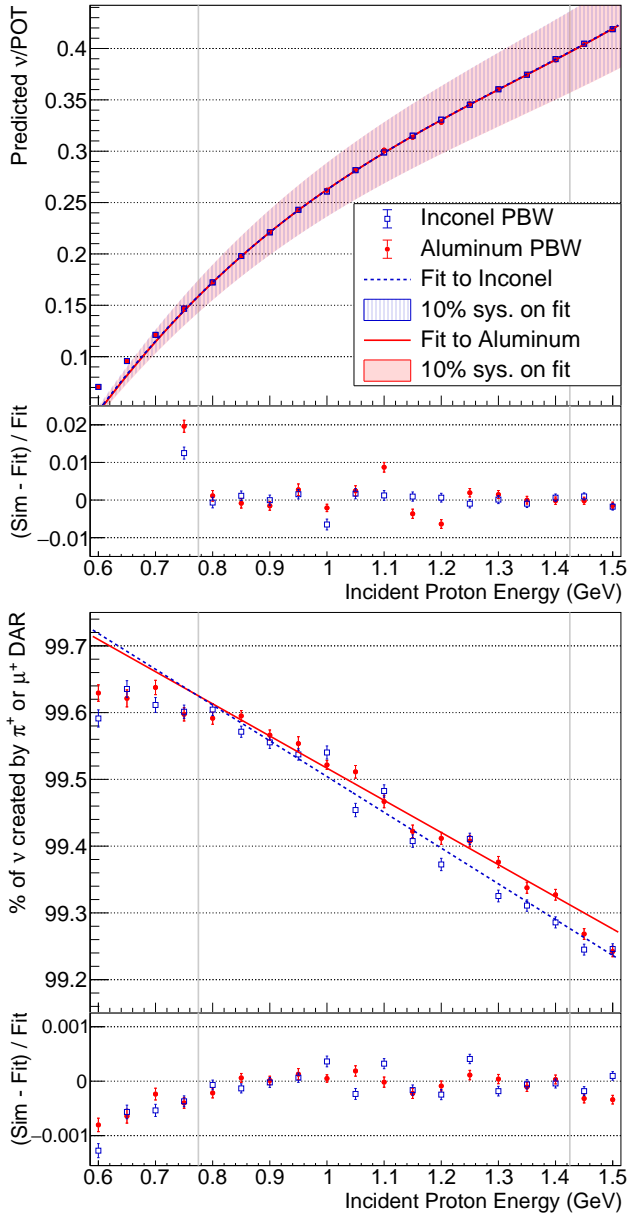


FIG. 11. Top: The total neutrino flux from the SNS will depend on the incident proton energy, and each operational configuration demonstrates a cubic dependence on this parameter. Bottom: The fraction of neutrinos produced from decay-at-rest processes demonstrates a linear dependence on the incident proton energy above ~ 0.8 GeV. The fit range for both plots is $E \in [0.775, 1.425]$ GeV; this is the region between the vertical gray lines. The bottom panel in each plot shows the relative residuals, calculated as in the axis label from the simulation (“Sim”) and fit (“Fit”) predictions.

materials which create the pions were listed in Table I; the neutrinos are primarily produced after the short movements of pions and muons coming to rest. The spread of the beam and the movements of the particles result in a radial spread from the beamline axis. Over 86% of the neutrinos are produced within 10 cm of the beamline

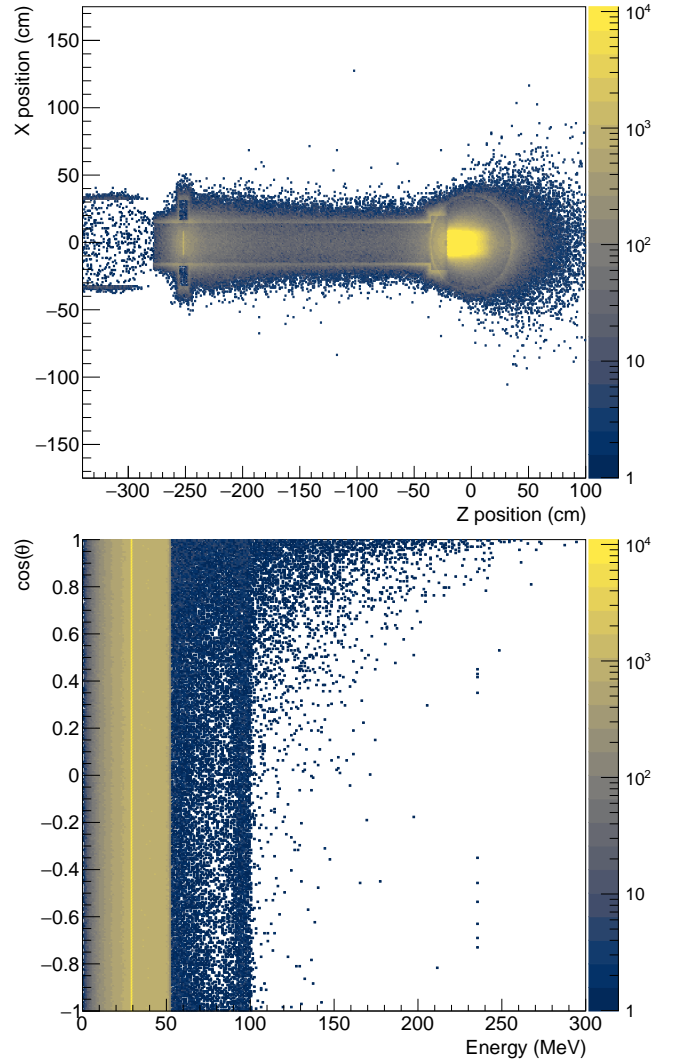


FIG. 12. Top: A top-down view of the neutrino creation positions. Bottom: Distribution of the kinetic energies and production angles (relative to the beamline axis without convolving the creation position information from the top panel) of all neutrinos.

axis, and almost all production ($>99\%$) occurs within 0.5 m of the beamline axis. Along the beamline axis, we find that over 90% of the neutrino production occurs within the target and less than 5% of the neutrinos are produced at the PBW location 2.5 m upstream of the target. Because the π^+ and μ^+ decay at rest, we also have almost fully isotropic production of neutrinos up to about 50 MeV. We do note visible anisotropy in the bottom panel of Fig. 12 for $E_\nu > 60$ MeV that is consistent with neutrinos boosted in the forward direction from pions decaying in flight.

We find that both PBW designs cause some neutrino production outside of the target regardless of the incident proton energy as illustrated in Fig. 13. However, our detectors are deployed ~ 20 m from the target center, with the PBW placement only 2.5 m upstream of the target.

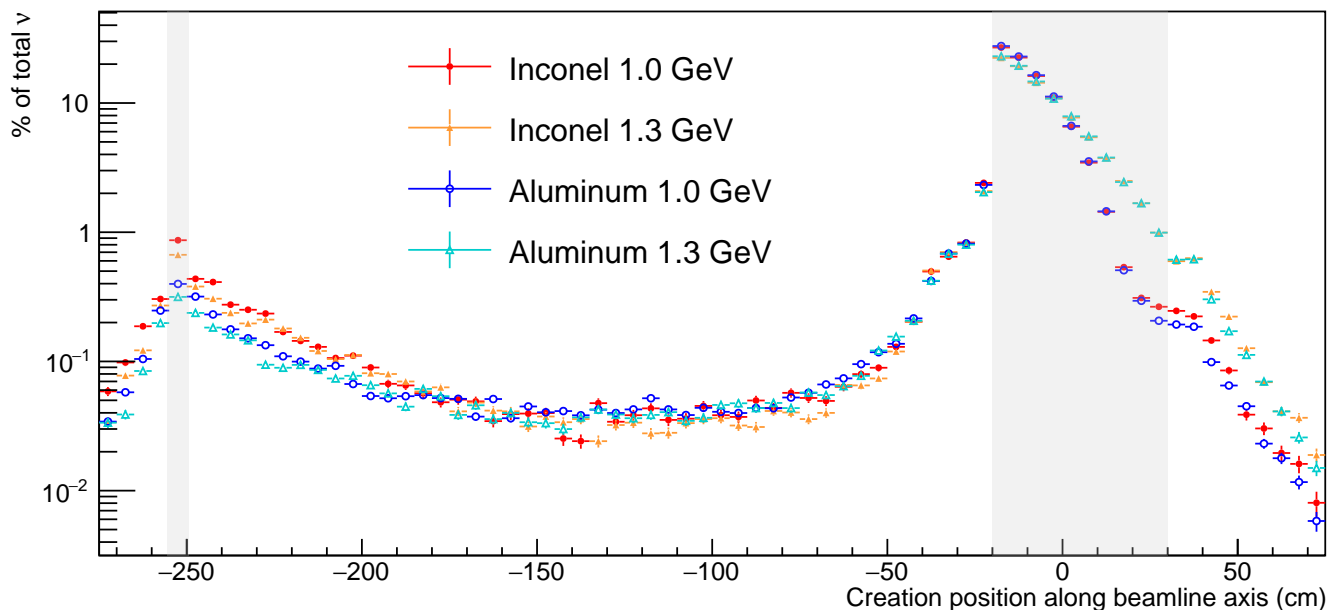


FIG. 13. A comparison of neutrino production along the beamline for different SNS configurations and beam energies. The gray shading to the left indicates the position of the proton beam window, and the shading to the right indicates the position of the Hg target.

To quantify the effect of this non-point-like neutrino production, we project the neutrino flux onto a 20 m sphere centered on the Hg target and determine an effective production angle based on the neutrino's projected location. In this model, the total anisotropy of the SNS neutrino flux 20 m from the target center is $\sim 5\%$. The dominant contribution is an excess near $\cos\theta \approx -1$ consistent with neutrino production within the PBW, with a secondary excess near $\cos\theta \approx 1$ consistent with neutrinos produced by decays in flight. For a small detector at the COH-CsI location 19.3 m from the target center and at $\cos\theta \approx 0$, we predict less than a 1% deficit of the neutrino flux compared to the isotropic point-source approximation. The contributions to the neutrino flux error from geometric considerations are small, and add negligibly in quadrature to the 10% to the overall neutrino flux incident on our detectors in Neutrino Alley. The anisotropy depends on the relative contributions of the different materials in our SNS geometry outlined in Table I, and emphasizes the need for new pion-production measurements such as those discussed in Section VII.

V. NEUTRINOS AT THE SECOND TARGET STATION

We also created a model geometry to estimate the neutrino production at ORNL's planned Second Target Station (STS) [56]. With a projected completion in the early 2030s, COHERENT is engaged with the design phase of this facility to optimize location and shielding with the aim to deploy 10-ton-scale detectors for CEvNS and other

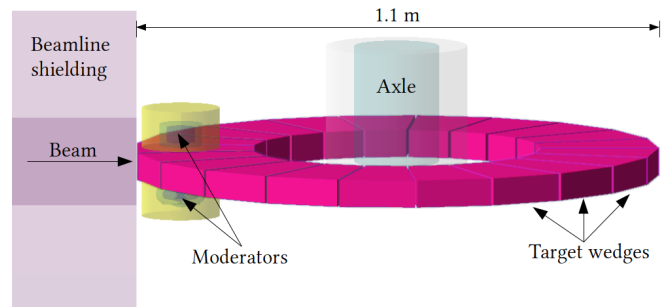


FIG. 14. Geant4 implementation of the Second Target Station target and moderators.

physics. Using preliminary details about the planned target provided at the Workshop on Fundamental Physics at the Second Target Station in 2019 [57], we modeled 21 tungsten wedges surrounded by thin layers of tantalum and water, evenly spaced in an assembly with a 1.1 m diameter. We also modeled neutron moderators above and below the active target wedge, centered along the beamline axis. We simulated a 6 cm (width) \times 5 cm (height) beam profile to ensure that the profile is smaller than that of a single tungsten wedge and included the aluminum PBW and beamline shielding as implemented in our First Target Station (FTS) geometry. This target geometry is illustrated in Fig. 14 and is centered inside a 5 m vacuum box, then enclosed in a steel box (10 m outer edge, 5 m inner) to mimic pion production in typical shielding materials without assuming the geometry of the STS target surroundings.

With this simple geometry and 1.3 GeV incident protons, our simulations predict $0.13 \nu_X / \text{POT}$ for $\nu_\mu, \bar{\nu}_\mu$, and ν_e from the π^+ decay chain, resulting in an approximate total $0.39 \nu / \text{POT}$. This estimate is larger than the predictions for the FTS operating at 1.3 GeV due to the increased density of a solid tungsten target. We cannot accurately discuss the decay-at-rest fraction of neutrinos or relative impact of the PBW since the shielding surrounding the target remains unknown. However, we note that protons do escape the end of the 25-cm thick active target wedge with enough energy to produce pions downstream of the target.

The STS will receive one of every four pulses from the SNS linear accelerator and will operate as a 15 Hz, 0.8 MW facility. Possible locations for 10-ton scale COHERENT detectors at the Second Target Station have been identified within a few tens of meters from the planned target location. With a tungsten target rather than mercury, hadron production experiments using a range of targets at lower beam energies will be useful in benchmarking our predictions [58].

VI. LIGHT DARK MATTER PRODUCTION AT THE SPALLATION NEUTRON SOURCE

This work was focused on understanding the neutrino fluxes but also explored the creation of other interesting particles. In particular, π^0 , η^0 , and π^- production are relevant to dark matter searches using the SNS as an accelerator [59, 60]. Here, we present some findings regarding the production of such particles using QGSP_BERT, noting that no effort was made in this work to specifically validate the production of any hadrons other than π^+ . As mentioned in Section II, η production is excluded from our discussion here because it is not predicted by QGSP_BERT. Predictions with QGSP_BIC have previously been used with this simulation geometry to predict η flux for sensitivity studies [60].

Figure 15 shows the scattering angle as it relates to the creation energy for SNS-produced π^0 from 1 GeV incident protons on the top and 1.3 GeV incident protons on the bottom. We observe strong forward production for both, but note that we will have a small flux directed towards Neutrino Alley ($\cos\theta \approx 0$). This is relevant primarily for the π^0 which could decay in flight into dark-matter particles that cause an observable nuclear recoil in our CEvNS detectors. For π^- , dark matter could be produced in an absorption process or in a charge-exchange process; both are more efficient at non-relativistic energies, and each would emit particles isotropically and negate any impact of forward production.

Assuming an aluminum PBW, the SNS produces $0.11 \pi^0/\text{POT}$ and $0.05 \pi^-/\text{POT}$ for 1 GeV incident protons. We also predict that the upgraded 1.3 GeV incident protons will produce $0.17 \pi^0/\text{POT}$ and $0.09 \pi^-/\text{POT}$. This study also demonstrates the potential gain of the STS for dark matter searches, particularly in aiming for forward-

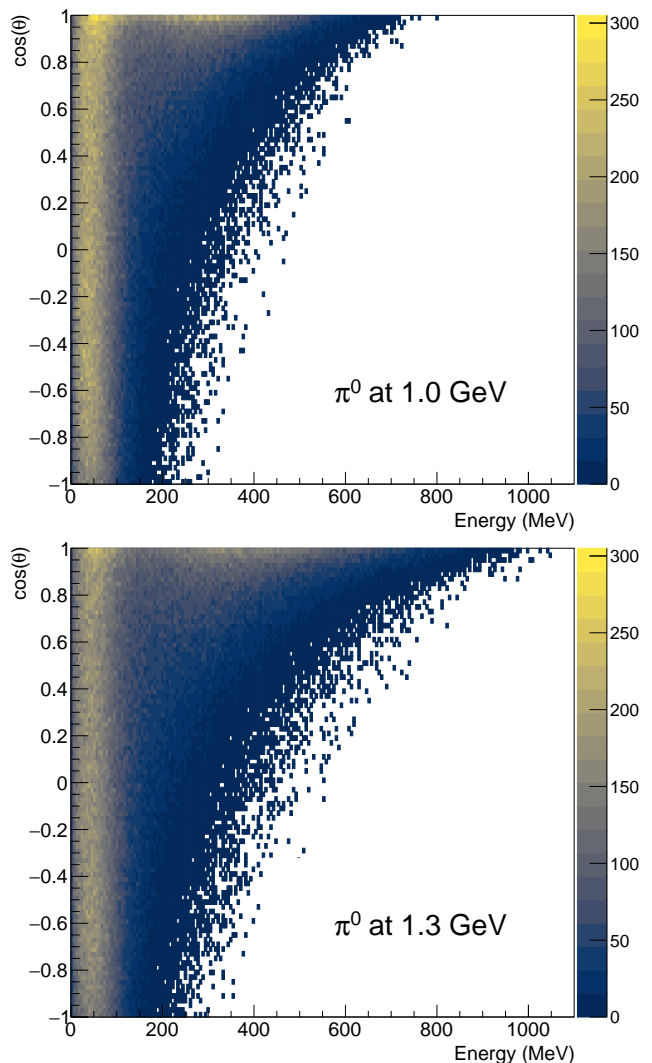


FIG. 15. Distribution of production angles and creation energies of π^0 at the SNS-FTS assuming an aluminum PBW. Top: Using 1 GeV incident protons to mimic the current operating conditions of the SNS. Bottom: Using 1.3 GeV incident protons to mimic the operating conditions following the upgrade.

positioned detectors that reduce the distance to the target.

VII. ONGOING EFFORTS

In the absence of either pion-production data for protons incident on Hg at energies up to 1.3 GeV or a precise measurement of the proton energy-loss profile within the SNS target, the $\sim 10\%$ uncertainty assigned to our neutrino flux is a robust estimate that cannot be significantly improved through simulation. Two types of experimental measurements could further reduce this uncertainty.

Pion-production measurements with thin Hg targets would allow us to validate our simulation against interactions on the same material as the SNS target. The

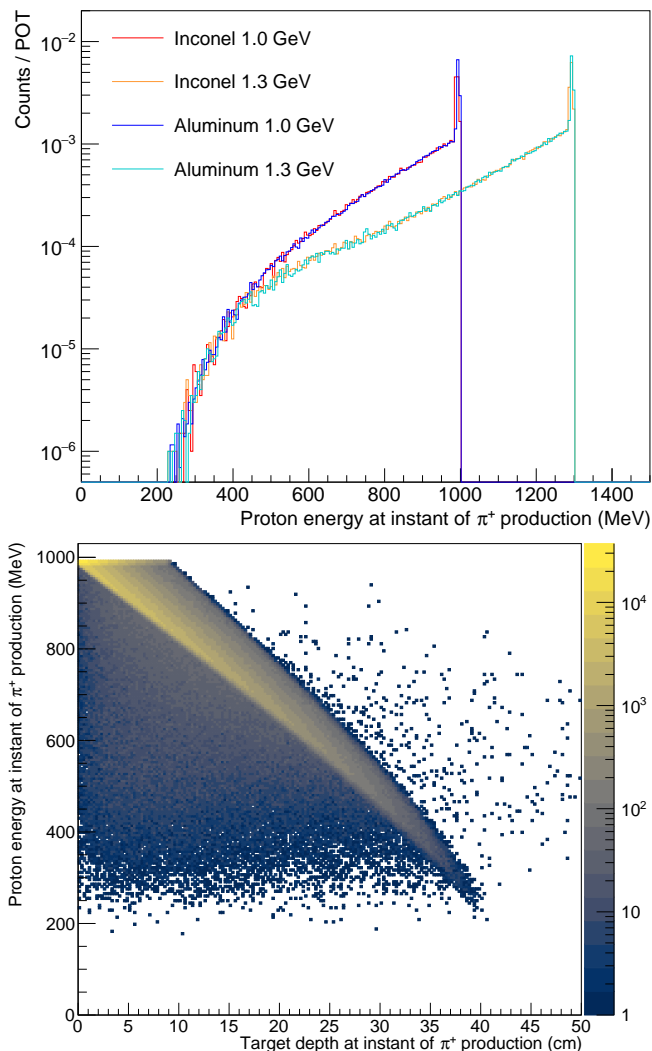


FIG. 16. Top: A histogram of the proton energies which produce π^+ at the SNS. Bottom: A closer look at how protons lose energy in the Hg target before creating π^+ .

proposed EMPHATIC experiment at the Fermilab Test Beam Facility could measure differential pion-production cross sections on Hg at proton energies as low as 2 GeV with expected uncertainties less than 10% [61]. Meanwhile, the NA61/SHINE collaboration [62], which has measured pion production on both thin and replica targets for a variety of accelerator neutrino experiments, is investigating the possibility of reducing the energy of the CERN SPS H2 proton beamline to 1 GeV for low-energy pion-production studies [63]. These measurements will benefit neutrino experiments at the SNS and at other pion decay-at-rest neutrino sources with GeV-scale protons incident on a mercury target such as the JSNS² sterile-neutrino search at the Japan Spallation Neutron Source [64]. As a decay-at-rest source is insensitive to the production angle of the pion, new pion-production measurements should ideally cover as close to a 4π acceptance as possible.

Thin-target data at ≥ 1 GeV, however, cannot account for the effects of proton energy loss in the SNS target and from scattering in the PBW as shown in Fig. 16. A separate approach to reducing neutrino flux uncertainties would directly measure the total neutrino production at the SNS target. A D₂O detector, deployed at the SNS, would measure the charged-current interaction

$$\nu_e + d \rightarrow p + p + e^- . \quad (5)$$

The cross section of this reaction is well understood; theoretical calculations, taking several disparate approaches, have converged to the 2–3% level [65, 66]. A moderately sized detector, about 680 kg, could achieve similar statistical precision in about four SNS beam-years of operation. The observed ν_e flux from the SNS target could then be multiplied by three to obtain the total flux of all three neutrino flavors generated by π^+ decay. The COHERENT collaboration plans to build such a detector to directly normalize the simulated SNS neutrino flux [67]. We note that if the neutrino flux can be independently measured to high precision, one can in principle use neutrino data to validate models of hadron and neutrino production.

VIII. CONCLUSIONS

Using Geant4.10.06’s standard QGSP_BERT physics list and treating the SNS as a point source, we predict a neutrino flux of $4.7 \times 10^7 \nu \text{ cm}^{-2} \text{ s}^{-1}$ at 20 m from the target with $\sim 99\%$ of the total flux produced by the stopped π^+ decay chain for 1 GeV incident protons at the 1.4 MW First Target Station. Our calculation has a 10% uncertainty on the underlying pion-production model. This shared systematic for all COHERENT detectors is now the dominant systematic uncertainty on our CEvNS measurements, along with statistics.

Our simulation remains an invaluable tool for estimating the flux of various particles at the SNS, the dependence of our predictions on the incident proton energy, and relative effects of the beamline geometry. In the future, we intend to use a modified version of this simulation to predict the low-energy contribution to the SNS neutrino flux from β^\pm decays coincident with a proton spill resulting from activated materials. We also intend to use the framework we have developed here to perform model validation studies for particles such as π^0 , π^- and η that are relevant for future dark matter studies at the SNS.

Acknowledgements

The COHERENT collaboration acknowledges the resources generously provided by the Spallation Neutron Source, a DOE Office of Science User Facility operated by the Oak Ridge National Laboratory. This work was

supported by the US Department of Energy (DOE), Office of Science, Office of High Energy Physics and Office of Nuclear Physics; the National Science Foundation; the Consortium for Nonproliferation Enabling Capabilities; the Institute for Basic Science (Korea, grant no. IBS-R017-G1-2019-a00); the Ministry of Science and Higher Education of the Russian Federation (Project “Fundamental properties of elementary particles and cosmology” No. 0723-2020-0041); and the US DOE Office of Science Graduate Student Research (SCGSR) program, administered for DOE by the Oak Ridge Institute for Science and Education which is in turn managed by Oak Ridge Associated Universities. The authors would also like to thank the Undergraduate Research Office of Carnegie Mellon

University for their support on this project. Sandia National Laboratories is a multi-mission laboratory managed and operated by National Technology and Engineering Solutions of Sandia LLC, a wholly owned subsidiary of Honeywell International Inc., for the U.S. Department of Energy’s National Nuclear Security Administration under contract DE-NA0003525. The Triangle Universities Nuclear Laboratory is supported by the U.S. Department of Energy under grant DE-FG02-97ER41033. Laboratory Directed Research and Development funds from Oak Ridge National Laboratory also supported this project. This research used the Oak Ridge Leadership Computing Facility, which is a DOE Office of Science User Facility.

-
- [1] J.R. Haines, T.J. McManamy, T.A. Gabriel, R.E. Battle, K.K. Chipley, J.A. Crabtree, L.L. Jacobs, D.C. Lousteau, M.J. Rennich, and B.W. Riemer, “Spallation neutron source target station design, development, and commissioning,” *Nuclear Instruments and Methods in Physics Research Section A: Accelerators, Spectrometers, Detectors and Associated Equipment* **764**, 94–115 (2014).
- [2] D. Akimov *et al.*, “Observation of coherent elastic neutrino-nucleus scattering,” *Science* **357** (2017).
- [3] D. Akimov *et al.* (COHERENT Collaboration), “First measurement of coherent elastic neutrino-nucleus scattering on argon,” *Phys. Rev. Lett.* **126**, 012002 (2021).
- [4] D. Akimov *et al.* (COHERENT collaboration), “COHERENT 2018 at the Spallation Neutron Source,” (2018), arXiv:1803.09183v2.
- [5] J. Barranco, O. G. Miranda, and T. I. Rashba, “Probing new physics with coherent neutrino scattering off nuclei,” *JHEP* **12**, 021 (2005).
- [6] Patrick deNiverville, Maxim Pospelov, and Adam Ritz, “Light new physics in coherent neutrino-nucleus scattering experiments,” *Phys. Rev. D* **92**, 095005 (2015).
- [7] P. Vogel and J. Engel, “Neutrino electromagnetic form factors,” *Phys. Rev. D* **39**, 3378–3383 (1989).
- [8] K. Scholberg, “Prospects for measuring coherent neutrino nucleus elastic scattering at a stopped-pion neutrino source,” *Phys. Rev. D* **73**, 033005 (2006).
- [9] J. Papavassiliou, J. Bernabeu, and M. Passera, “Neutrino-nuclear coherent scattering and the effective neutrino charge radius,” *Proceedings, 2005 Europhysics Conference on High Energy Physics (EPS-HEP 2005)*, PoS **HEP2005**, 192 (2006).
- [10] T. S. Kosmas *et al.*, “Probing neutrino magnetic moments at the spallation neutron source facility,” *Phys. Rev. D* **92**, 013011 (2015).
- [11] M. Cadeddu, C. Giunti, K. A. Kouzakov, Y. F. Li, A. I. Studenikin, and Y. Y. Zhang, “Neutrino charge radii from coherent elastic neutrino-nucleus scattering,” *Phys. Rev. D* **98**, 113010 (2018).
- [12] P. S. Amanik and G. C. McLaughlin, “Nuclear neutron form factor from neutrino-nucleus coherent elastic scattering,” *J. Phys. G* **36**, 015105 (2008).
- [13] Kelly Patton *et al.*, “Neutrino-nucleus coherent scattering as a probe of neutron density distributions,” *Phys. Rev. C* **86**, 024612 (2012).
- [14] M. Cadeddu *et al.*, “Average CsI neutron density distribution from COHERENT data,” *Phys. Rev. Lett.* **120**, 072501 (2018).
- [15] C. A. Duba *et al.*, “HALO – the helium and lead observatory for supernova neutrinos,” *J. Phys. Conf. Ser.* **136**, 042077 (2008).
- [16] D. Väänänen and C. Volpe, “The neutrino signal at HALO: learning about the primary supernova neutrino fluxes and neutrino properties,” *JCAP* **10**, 019 (2011).
- [17] K. Langanke, P. Vogel, and E. Kolbe, “Signal for supernova ν_μ and ν_τ neutrinos in water Čerenkov detectors,” *Phys. Rev. Lett.* **76**, 2629–2632 (1996).
- [18] K. Scholberg, “Supernova Neutrino Detection,” *Annu. Rev. Nucl. Part. Sci.* **62**, 81–103 (2012).
- [19] B. Abi, R. Acciarri, M. A. Acero, G. Adamov, D. Adams, M. Adinolfi, Z. Ahmad, J. Ahmed, T. Alion, S. Alonso Monsalve, and et al., “Supernova neutrino burst detection with the Deep Underground Neutrino Experiment,” *The European Physical Journal C* **81** (2021), 10.1140/epjc/s10052-021-09166-w.
- [20] D. Akimov *et al.* (COHERENT collaboration), “Measurement of the Coherent Elastic Neutrino-Nucleus Scattering Cross Section on CsI by COHERENT,” (2021), arXiv:2110.07730.
- [21] S. Agostinelli *et al.* (GEANT4), “GEANT4: A Simulation toolkit,” *Nucl. Instrum. Meth.* **A506**, 250–303 (2003).
- [22] J. Allison *et al.*, “Geant4 developments and applications,” *IEEE Trans. Nucl. Sci.* **53**, 270 (2006).
- [23] D. Akimov *et al.* (COHERENT collaboration), “A Geant4 simulation of particle production at the Spallation Neutron Source,” (2022), <https://doi.org/10.5281/zenodo.6391623>.
- [24] Hugo W. Bertini, “Intranuclear-Cascade Calculation of the Secondary Nucleon Spectra from Nucleon-Nucleus Interactions in the Energy Range 340 to 2900 MeV and Comparisons with Experiment,” *Phys. Rev.* **188**, 1711–1730 (1969).
- [25] D.H. Wright and M.H. Kelsey, “The geant4 bertini cascade,” *Nuclear Instruments and Methods in Physics Research Section A: Accelerators, Spectrometers, Detectors and Associated Equipment* **804**, 175–188 (2015).
- [26] G. Folger, V. N. Ivanchenko, and J. P. Wellisch, “The Binary Cascade,” **21**, 407–417 (2004).

- [27] A. Boudard, J. Cugnon, J.-C. David, S. Leray, and D. Mancusi, “New potentialities of the liège intranuclear cascade model for reactions induced by nucleons and light charged particles,” *Phys. Rev. C* **87**, 014606 (2013).
- [28] S. Leray *et al.*, “Results from the iaea benchmark of spallation models,” *Journal of the Korean Physical Society* **59**, 791–796 (2011).
- [29] S. Leray, D. Mancusi, P. Kaitaniemi, J. C. David, A. Boudard, B. Braunn, and J. Cugnon, “Extension of the liège intra nuclear cascade model to light ion-induced collisions for medical and space applications,” *Journal of Physics: Conference Series* **420**, 012065 (2013).
- [30] Richard E. Prael and Henry Lichtenstein, “User Guide to LCS: The LAHET Code System,” LA-UR-89-3014 (1989).
- [31] R.L. Burman and P. Plischke, “Neutrino fluxes from a high-intensity spallation neutron facility,” *Nuclear Instruments and Methods in Physics Research Section A: Accelerators, Spectrometers, Detectors and Associated Equipment* **398**, 147–156 (1997).
- [32] R.L. Burman, A.C. Dodd, and P. Plischke, “Neutrino flux calculations for the isis spallation neutron facility,” *Nuclear Instruments and Methods in Physics Research Section A: Accelerators, Spectrometers, Detectors and Associated Equipment* **368**, 416–424 (1996).
- [33] R.L. Burman, M.E. Potter, and E.S. Smith, “Monte carlo simulation of neutrino production by medium-energy protons in a beam stop,” *Nuclear Instruments and Methods in Physics Research Section A: Accelerators, Spectrometers, Detectors and Associated Equipment* **291**, 621–633 (1990).
- [34] D. R. F. Cochran, P. N. Dean, P. A. M. Gram, E. A. Knapp, E. R. Martin, D. E. Nagle, R. B. Perkins, W. J. Shlaer, H. A. Thiessen, and E. D. Theriot, “Production of charged pions by 730-mev protons from hydrogen and selected nuclei,” *Phys. Rev. D* **6**, 3085–3116 (1972).
- [35] J. F. Crawford, M. Daum, G. H. Eaton, R. Frosch, H. Hirschmann, R. Horisberger, J. W. McCulloch, E. Steiner, R. Hausammann, R. Hess, and D. Werren, “Measurement of cross sections and asymmetry parameters for the production of charged pions from various nuclei by 585-mev protons,” *Phys. Rev. C* **22**, 1184–1196 (1980).
- [36] John W. Norbury and Lawrence W. Townsend, “Parameterized total cross sections for pion production in nuclear collisions,” *Nuclear Instruments and Methods in Physics Research Section B: Beam Interactions with Materials and Atoms* **254**, 187–192 (2007).
- [37] M.G. Catanesi *et al.* (HARP), “The HARP detector at the CERN PS,” *Nucl. Instrum. Meth. A* **571**, 527–561 (2007).
- [38] V.V. Abaev, E.P. Fedorova-Koval, A.B. Gridnev, V.P. Koptev, S.P. Kruglov, Yu.A. Malov, G.V. Shcherbakov, I.I. Strakovsky, and N.A. Tarasov, “Inclusive Pion Production at the Angles 0-degrees and 57.8-degrees in 1-{GeV} Proton Nucleus Collisions,” *J. Phys. G* **14**, 903–929 (1988).
- [39] S. Nagamiya, M. C. Lemaire, E. Moeller, S. Schnetzer, G. Shapiro, H. Steiner, and I. Tanihata, “Production of pions and light fragments at large angles in high-energy nuclear collisions,” *Phys. Rev. C* **24**, 971–1009 (1981).
- [40] A. Bolshakova *et al.* (HARP-CDP), “On the flaws in ‘Official’ HARP’s data analysis,” (2008), <https://cds.cern.ch/record/1137133/files/SPSC-SR-037.pdf>.
- [41] A. Bolshakova *et al.* (HARP), “Cross-Sections of Large-Angle Hadron Production in Proton- and Pion-Nucleus Interactions V: Lead Nuclei and Beam Momenta from +3 GeV/c to +15 GeV/c,” *Eur. Phys. J. C* **66**, 57–117 (2010).
- [42] M.G. Catanesi *et al.* (HARP), “Large-angle production of charged pions by 3-GeV/c - 12-GeV/c protons on carbon, copper and tin targets,” *Eur. Phys. J. C* **53**, 177–204 (2008).
- [43] A. Bolshakova *et al.* (HARP-CDP), “Cross-sections of large-angle hadron production in proton- and pion-nucleus interactions VI: carbon nuclei and beam momenta from ± 3 GeV/c to ± 15 GeV/c,” *Eur. Phys. J. C* **70**, 573–633 (2010).
- [44] A. Bolshakova *et al.*, “Cross-sections of large-angle hadron production in proton- and pion-nucleus interactions VIII: aluminium nuclei and beam momenta from ± 3 GeV/c to ± 15 GeV/c,” *Eur. Phys. J. C* **72**, 1882 (2012).
- [45] A. Bolshakova *et al.*, “Cross-sections of large-angle hadron production in proton- and pion-nucleus interactions VII: tin nuclei and beam momenta from ± 3 GeV/c to ± 5 GeV/c,” *Eur. Phys. J. C* **71**, 1719 (2011).
- [46] M.G. Catanesi *et al.* (HARP), “Large-angle production of charged pions with 3-12.9-GeV/c incident protons on nuclear targets,” *Phys. Rev. C* **77**, 055207 (2008).
- [47] A. Bolshakova *et al.* (HARP-CDP), “Cross-Sections of Large-Angle Hadron Production in Proton- and Pion-Nucleus Interactions. III. Tantalum Nuclei and Beam Momenta from +3 GeV/c to +15 GeV/c,” *Eur. Phys. J. C* **63**, 549–609 (2009).
- [48] A. Bolshakova *et al.* (HARP), “Cross-Sections of Large-Angle Hadron Production in Proton- and Pion-Nucleus Interactions V: Lead Nuclei and Beam Momenta from +3 GeV/c to +15 GeV/c,” *Eur. Phys. J. C* **66**, 57–117 (2010).
- [49] L. Aliaga *et al.*, “Neutrino flux predictions for the numi beam,” *Physical Review D* **94** (2016), 10.1103/physrevd.94.092005.
- [50] Ethan Tuttle, “Updating hadron production models to better predict neutrino flux for dune,” (2020), 10.2172/1661678.
- [51] ORNL (private communication), “Spallation Neutron Source Manufacturing Study Drawings,” (2015).
- [52] Special Metals, “Technical Bulletins for INCONEL Alloys,” (2021).
- [53] S. Henderson *et al.*, “The spallation neutron source accelerator system design,” *Nuclear Instruments and Methods in Physics Research Section A: Accelerators, Spectrometers, Detectors and Associated Equipment* **763**, 610–673 (2014).
- [54] Willem Blokland, T McManamy, and T Shea, “SNS target imaging system software and analysis,” *Proc. BIW10, Santa Fe, New Mexico, US* (2010).
- [55] J. Galambos, D. Anderson, C. Barbier, K. Bekar, D. Bunch, Jr. H. Bullman, and M. Buchanan, “Conceptual Design Report: Proton Power Upgrade Project,” (2017).
- [56] D. Anderson *et al.*, “Technical Design Report: Second Target Station,” ORNL/TM-2015/24 (2015).
- [57] “Workshop on Fundamental Physics at the Second Target Station (FPSTS19),” (July 2019), <https://conference.sns.gov/event/171/>.

- [58] J. Asaadi *et al.*, “Neutrino Opportunities at the ORNL Second Target Station,” (August 2020), Snowmass whitepaper.
- [59] Bhaskar Dutta, Doojin Kim, Shu Liao, Jong-Chul Park, Seodong Shin, and Louis E. Strigari, “Dark matter signals from timing spectra at neutrino experiments,” *Phys. Rev. Lett.* **124**, 121802 (2020).
- [60] D. Akimov *et al.*, “Sensitivity of the coherent experiment to accelerator-produced dark matter,” *Phys. Rev. D* **102**, 052007 (2020).
- [61] T. Akaishi *et al.*, “EMPHATIC: A proposed experiment to measure hadron scattering and production cross sections for improved neutrino flux predictions,” (2019), arXiv:1912.08841.
- [62] N. Abgrall *et al.* (NA61/SHINE), “NA61/SHINE facility at the CERN SPS: beams and detector system,” *JINST* **9**, P06005 (2014).
- [63] “NA61/SHINE at Low Energy,” (December 2020).
- [64] S. Ajimura *et al.* (JSNS²), “Technical Design Report: Searching for a Sterile Neutrino at J-PARC MLF,” arXiv:1705.08629.
- [65] B. Mosconi *et al.*, “Model dependence of the neutrino-deuteron disintegration cross sections at low energies,” *Phys. Rev. C* **75**, 044610 (2007).
- [66] Shung-Ichi Ando, Young-Ho Song, and Chang Ho Hyun, “Neutrino-deuteron reactions at solar neutrino energies in pionless effective field theory with dibaryon fields,” *Phys. Rev. C* **101**, 054001 (2020).
- [67] D. Akimov *et al.*, “A D₂O detector for flux normalization of a pion decay-at-rest neutrino source,” *Journal of Instrumentation* **16**, P08048 (2021).